



Geometry evolution prediction and process settings influence in profiled ring rolling

Irene Mirandola¹ · Luca Quagliato² · Guido A. Berti¹ · Roberto Caracciolo¹ · Seok Chang Ryu² · Mattia Perin³ · Naksoo Kim⁴

Received: 1 February 2022 / Accepted: 9 August 2022 / Published online: 17 August 2022
© The Author(s), under exclusive licence to Springer-Verlag London Ltd., part of Springer Nature 2022

Abstract

A kinematic-based analytical model was developed for estimating the geometrical expansion of profiled rings during the ring rolling process and validated against own and literature experimental results. The model, based on the volume conservation principle, describes the material redistribution between radial and circumferential directions due to the employed process parameters and friction conditions. The comparison between analytical and experimental ring diameters evolutions, carried out considering various materials, process conditions, and profiled ring shapes, showed maximum and average deviations equal to 4.9% and 2.1%, proving the reliability of the implemented kinematic solution. The penetration and biting-in conditions, well-known in flat ring rolling, showed to be applicable and effective also in profiled ring rolling, allowing to define the suitable ranges for the mandrel feeding speed and the main roll rotation speed. The proposed solution was utilized, coupled with thermo-mechanical FEM simulations, to investigate the influence of the ring preform shape and the process parameters on the geometrical expansion of both wall and flange of the ring during the process. Furthermore, the range of validity of the developed analytical model was investigated as well.

Keywords Profiled ring rolling · Process parameters · Analytical model · Geometry expansion prediction · Thermo-mechanical FEM model

Abbreviations

ω_R	Main roll rotation speed
R_R	Main roll radius
R_M	Mandrel radius
$[v_M]_0, [v_M]_F$	Initial and final mandrel feeding speed ranges
β_R	Friction angle

R_0	Ring preform outer radius
r_0	Ring preform inner radius
R_F	Final ring outer radius
r_F	Final ring inner radius
$R_{w,0}, R_{w,i}, R_{w,i+1}$	Profiled ring wall radius (initial, i-round, and i + 1 round)
$s_{w,0}, \bar{s}_{w,i}, \bar{s}_{w,i+1}$	Profiled ring thickness (initial, i-round, and i + 1 round)
t_1	Mandrel time for the first round of the process
t_i, t_{i+1}	Mandrel time for the i-round and the i + 1 round
t_j	Generic process time within the mandrel feeding time
$V_{w,0}, V_{w,i}$	Ring wall volume (Initial and i-round)
$R_{in,0}, R_{in,i}$	Ring inner radius (Initial and i-round)
h_w, h_f	Ring wall and ring flange heights
λ	Wall-flange height factor
\bar{R}_{wc}	Average radius of the ring wall
R_f	Radius of the ring flange
τ	Friction stress
k	Yield strength

Irene Mirandola and Luca Quagliato equally contributed to this work.

✉ Luca Quagliato
lucaq@ewha.ac.kr

✉ Naksoo Kim
nskim@sogang.ac.kr

¹ Department of Management and Engineering, University of Padua, 36100 Vicenza, Italy
² Division of Mechanical and Biomedical Engineering, Ewha Womans University, 03760 Seoul, Republic of Korea
³ Zamperla S.P.A, 36077 Vicenza, Italy
⁴ Department of Mechanical Engineering, Sogang University, 04107 Seoul, Republic of Korea

m	Friction factor
v	Velocity parameter

1 Introduction

The ring rolling is a well-established manufacturing process in which an initial ring preform is deformed in both thickness and height toward a final shape with a thinner thickness and lower height but greater inner and outer diameters [1]. Due to its versatility, energy efficiency, favorable grain orientation, and absence of weld lines, ring rolling is utilized to manufacture components in several industrial sectors, such as heavy machinery, aerospace, and wind generation [2].

Depending on the final shape, the process can be subdivided into a flat (plane) ring rolling for an annular shape without protrusions and a profiled ring rolling when the cross-section is not rectangular but presents flanges or grooves [3]. For the past 50 years, most research has focused on investigating the former through analytical models to understand the basic mechanics of the process, finite element method (FEM) simulations, and both laboratory-scale and industrial-scale experiments.

Regarding the analytical models, Lin and Zhi [4] defined the range for mandrel feeding speed to achieve full plastic deformation throughout the whole thickness of the ring (*penetration condition*) and prevent the ring from stopping its rotation due to too high friction in the deformation gap (*biting-in condition*). Zhou et al. [5] improved this solution by adding the mutual interaction between the radial and axial deformations but considered a constant mandrel speed during the process. Afterward, Berti et al. [1] proposed a linearly decreasing mandrel feeding speed approach, improving the sets of equations proposed in [4, 5]. This modeling allowed achieving remarkably high stability during the process and an excellent agreement between FEM and analytical results. Based on [1], Quagliato and Berti investigated the variation of the 3D strain field in the ring during the process [6], defining the relevant material flow, and developed two analytical force models. The former [7] is specifically designed for the ring rolling process, and the latter [8], based on the slip line theory, and employable in any forming process where a circumferential arc defines the tool-working contact.

Concerning the FEM modeling, hybrid computational-material meshing systems have been utilized by Lim et al. [9] to reduce the computational time, while an arbitrary Lagrangian–Eulerian formulation has been employed by Davey and Ward [10] to reduce the number of integration steps required in ring rolling FEM simulations. More recently, Kim et al. [11] defined a dual-meshing strategy to achieve a coarser mesh for the portion of the ring outside the deformation gap and a fine mesh only for the

element within it. Besides, Kim et al. [12] developed an FEM program named SHAPE-RR[®] and utilized it, along with industrial experiments, to define a procedure for minimizing the load in the ring rolling process based on the conjugate-gradient technique and Taguchi method. FEM simulations have also been utilized by Berti et al. [1], Zhou et al. [5], Quagliato and Berti [6–8], Guo and Yang [13], Parvizi and Abrinia [14], and Anjami and Basti [15], for the validation of analytical models developed for process control, force, and geometry prediction. On top of that, hybrid FEM-experimental modeling has been developed by Jenkouk et al. [16] in terms of a closed-loop Abaqus VUAMP subroutine to control the motion of the tools of the ring rolling mill during the process. This procedure can better follow the inevitable deviations arising during the rolling process, thus proposing a better real-time correction of the tool motion rules to achieve the required final shape. Similarly, Liang et al. [17] utilized an integrated Abaqus/explicit-based process control in which the process settings are continuously adjusted to keep the workpiece temperature in a pre-specified range, thus granting a constant ring growth velocity, suitable microstructure, and few forging defects.

Regarding the profiled ring rolling process, whose complexity is far greater than the flat ring rolling [18–20], most of the contributions available deal with experimental investigations or FEM development, and only a few are related to analytical modeling of the profiled ring rolling process. Qian et al. [21] defined the admissible velocity field equations based on the minimum resistance principle to achieve deep grooves starting from a flat ring preform. The model has been validated against FEM and experimental results, but the geometrical accuracy of the ring is not investigated. Deng and Mao [22] investigated the plastic flow from a rectangular to a profiled cross-section and proposed an analytical model for the definition of a preform that accounts for possible material loss during production.

Zhou et al. [23] investigated the possibility of creating an axial flange, created by the axial rolls, and developed an algorithm for the estimation of the ring geometry evolution through the process. The model has been validated against previously published experiments and FEM results and showed to be able to follow the trend of the relevant FEM simulation, but no detailed information on the time-dependent expansion of the ring shape is provided. Finally, Qian et al. [24] proposed an interesting analysis of the gripping conditions for profiled rings, which ensures the above penetration and biting-in conditions. A similar approach, based on [1], is also employed in this paper.

For the preform design in profiled ring rolling, Alfozan and Gunasekera [25] utilized the Upper Bound Elemental Technique (UBET) for estimating the initial ring shape, minimizing the energy rate, and coupled it with backward

tracing simulations. Qian and Hua [26] utilized a combined analytical-FEM solution to determine the ring preform shape to reach the final desired cross-section. Besides, Zhao and Qian [27] investigated the correlation between the rolling ratio, defined as the cross-sectional area of the blank to that of the final ring, and proposed a methodology for calculating the admissible ratio to achieve uniform deformation in the ring cross-section. Concerning the FEM analysis of the profiled ring rolling process, Davey and Ward [28, 29] defined a technique based on the arbitrary Lagrangian–Eulerian (ALE) formulation to reduce computation time. Good accuracy for small deformation while a greater deviation, in comparison to the relevant experiment, is observed for larger diameter growth. Similar hybrid mesh approaches are also utilized in [9, 30, 31].

Kim et al. [32] defined a finite element model predicting the geometrical expansion of side- and top-grooved rings, showing a time-dependent evolution of the cross-section for each process revolution in a sort of flower pattern chart. Similarly, Ranatunga et al. [33] implemented an Upper Bound Elemental Technique (UBET) to simulate the profiled ring rolling process, showing good agreement with the experimental results for complex ring geometries utilized in the aerospace industry. As concerns the utilization of commercial FEM solutions, several studies presented 3D-thermo-mechanical FEM models based on the Abaqus/explicit environment and used them for the investigation of the plastic deformation field developing in the ring cross-section during the process [34–37], for the estimation of the process force [38], and the estimation of the geometrical evolution of the ring [21]. Furthermore, the commercial software FORGE has also been utilized to investigate the process parameter influence on force and geometry evolution [39] and to analyze the blank dimensions on the geometrical accuracy of conical rings made of Inconel 718 alloy [40]. The FEM technique has also been utilized to investigate industrially relevant studies, such as by Monti and Berti [41] for optimizing the process of a flanged ring made of 42CrMo4 steel used in a power generation plant, in Lee et al. [42] for defining the multi-stage ring rolling process for an excavator idle rim made of AISI-1035 steel, and in Park et al. [43] for designing the initial blank to be utilized in the profiled ring rolling process of rings employed in construction machines. In addition, the issue of the preform design has been investigated by Tani et al. [44], where the weight of the final part was reduced by 55% thanks to a combined optimization of both metallurgical and manufacturing processes.

In addition to that, several studies dealt with lab-scale and industrial-scale experimental investigations. Cleaver et al. [45] defined a ring rolling machine setting and control procedure for creating profiled rings with variable thickness. Cleaver and Allwood [46] utilized a 12-axis rolls machine to manufacture flat and L-shape profiled rings, proving that

a high number of constraints along axial and circumferential directions allow for improving both profile shape and circularity. Cleaver et al. [47] also investigated the possibility, and the relevant forming limits, of creating L-shape rings with no circumferential growth to maximize the flange expansion. Moreover, Cleaver and Allwood [48] employed laboratory-scale experiments to investigate the possibility of creating inner and outer tapered angles during the ring rolling process, thus allowing for less post-op reworking and material waste.

In terms of process control, Li et al. [49] defined an FEM-driven system for controlling the guide rolls during the ring rolling process and applied it to a profiled AA-2219 ring. Additionally, Oh et al. [50] investigated the contact between ring and tools in the profiled ring rolling process and defined the contact conditions leading to unfilling in some areas of the part. The developed FEM model was afterward utilized for optimizing an industrial case ring, where a significant improvement in the filling quality was observed. Finally, Li et al. [51] proposed a variable setting methodology for the feed rates during the profiled ring rolling to improve process control and utilize it for process optimization.

As summarized, several studies focused on the flat and profiled ring rolling process, especially numerical simulation model development and experimental investigations. However, two issues relevant to the profiled ring rolling process seem to be not fully investigated in the literature. The former concerns the prediction of the geometrical expansion of the ring during the process, whereas the former is relevant to the connection between the process parameters settings and the geometrical expansion of the ring during the process. Especially, a systematic investigation of how different process parameters influence the plastic flow in the ring cross-section and circumferential direction seems to be missing in the literature. The matter of set-up for the profiled ring rolling process presents an additional issue of the material redistribution during the forming, which might lead to overgrowing of the circumference at the expense of an undergrowing the flange. This issue has been partially investigated by Kang [52] for three specific C-Shape, L-shape, and not symmetric C-shape ring geometries. Still, no clear correlation with the process variables is discussed. Similarly, Liang et al. [53] investigated the influence of the preform shape for C-grooved rings and defined a forming criterion, based on the so-called pulling coefficients, to limit the circumferential expansion and achieve a better flange growth.

Following the issues highlighted so far, this research presents an analytical model for the estimation of the geometrical growth of the ring during the profiled ring rolling process and is based on a kinematic assumption coupled with the volume conservation principle. If the ring expands quickly enough, the temperature drop in the majority of the ring cross-section can be assumed to be small; thus,

the resistance to plastic deformation can be assumed to be constant, and the geometrical expansion is regarded as a kinematic problem. This assumption is valid for hot forming conditions or low hardening material. Within this scenario, the proposed analytical model is meant as an initial screening tool, allowing process engineers to investigate the influence of various sets of process parameters and preform geometries on the geometrical expansion of the ring as well as a pre-step to FEM simulations, utilized for the final tuning of the process. The developed analytical model is not intended as a replacement for FEM simulations but as a tool for minimizing the high computational effort required for the thermo-mechanical FEM model generally utilized for the ring rolling process.

The analytical model has been developed considering a cylindrical ring preform to avoid bias, but it can also be extended to already-profiled ring preforms. As discussed throughout the paper, the model applies to any flange type, including inner L-shape, outer L-shape, and C-shape (double symmetric L-shape). The analytical model has been validated against previous literature studies relevant to inner flange [46], outer flange [48], and C-grooved rings [53], showing good agreement with the experimental results and the generality of the model. Furthermore, both the developed analytical model and the employed FEM simulation have been validated against the authors' previous experimental results, partially presented in [41], and relevant for a ring made of 42CrMo4 steel.

Two additional analyses have also been carried out to investigate the performances of the developed analytical model and to establish the correlation between the initial and final shapes of the ring, its geometrical evolution, and the relevant process parameters. For the former, three different initial and final ring configurations have been coupled with three different main roll rotational speeds, for a total of 27 cases. This first analysis aims to understand the influence of the main roll rotational speed and the initial and final mandrel feeding speeds on the geometrical expansion of the ring during the process. For the latter, the same initial preform shape has been utilized for manufacturing various profiled rings with different

final shapes, allowing for investigating the correlation between process parameters and material flow redistribution in the cross-section of the ring. The second investigation is applied to two different metallic materials, the 42CrMo4 steel and the Inconel 718 superalloy, to validate the above-mentioned kinematic assumption, whose results will show that, if the process is properly set up, the variation of the material flow stress resistance, caused by the temperature drop, is limited and remarkably similar geometrical expansions can be achieved regardless of the material employed.

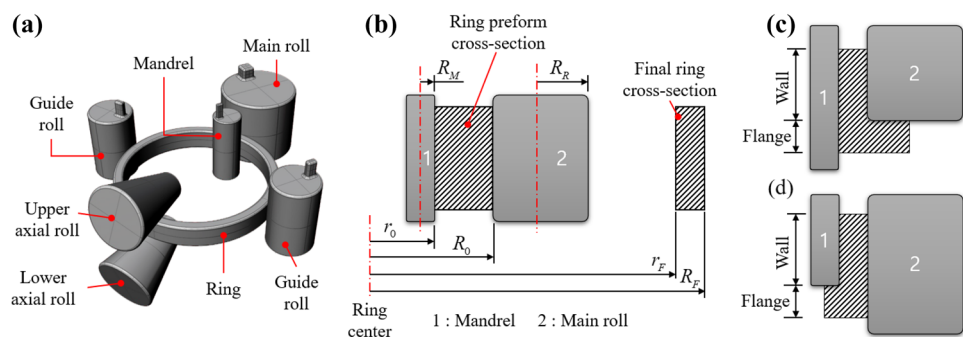
2 Process control parameters ranges and geometric expansion modeling

This section is devoted to the description of the process parameter ranges for the profiled ring rolling process and a detailed explanation of the proposed analytical model for the estimation of the geometrical evolution of the profiled ring diameters throughout the process.

2.1 Process control parameters

In the flat ring rolling process, Fig. 1a [54], the mandrel applies a uniform deformation toward the ring thickness, resulting in a circumferential expansion, Fig. 1b, and an indirect increase of the height, afterward controlled by the axial rolls [6]. For the profiled ring rolling process of external flange rings, Fig. 1c, the mandrel applies its pressure on the whole ring height whereas the main roll is only on the ring wall. In the same way, for internal flanges (Fig. 1d), the mandrel is not acting on the whole height of the ring, but only on the portion not related to the flange. In general, the ring wall has a controlled deformation, and the contact conditions are remarkably similar to those of the flat ring rolling process [1, 4, 5]. For this typology of contact, the same forming limit conditions to achieve full plastic deformation throughout the whole thickness (*penetration condition*) and to avoid the jamming of the ring in the deformation gap (*biting-in condition*) must be satisfied.

Fig. 1 a Schematic representation of the ring rolling process. Contact conditions between mandrel, main roll, and ring for b flat ring, c external flange, and d internal flange in profiled rings



By considering a linearly decreasing mandrel feeding speed from the beginning to the end of the process, excluding the calibration phase, the admissible ranges for the initial and final mandrel feeding speeds can be set according to the conditions defined in [1] for the case of flat rings, Eqs. (1)–(3).

The parameters of Eqs. (1)–(3) are summarized in the nomenclature table, and some are displayed in Fig. 1b. The friction angle is calculated based on the friction factor as $\beta_R = \tan^{-1}(m)$. Under the contact conditions shown in Fig. 1b, the controlled expansion of the ring wall is set to fulfill both conditions mentioned above and is, in principle, the same as that of flat rings.

$$\frac{\omega_R \cdot R_R \cdot 6.55 \cdot 10^{-3} \cdot (R_0 - r_0)^2 \cdot S_1}{2\pi \cdot R_0} < [v_M]_0 < \frac{\omega_R \cdot R_R \cdot \beta_R^2 \cdot S_1}{\pi \cdot R_0 \cdot (S_3)^2} \tag{1}$$

$$\frac{\omega_R \cdot R_R \cdot 6.55 \cdot 10^{-3} \cdot (R_F - r_F)^2 \cdot S_2}{2 \cdot \pi \cdot R_F} < [v_M]_F < \frac{\omega_R \cdot R_R \cdot \beta_R^2 \cdot S_2}{\pi \cdot R_F \cdot (S_3)^2} \tag{2}$$

$$\text{where } S_1 = \frac{1}{R_R} + \frac{1}{R_M} + \frac{1}{R_0} + \frac{1}{r_0}; S_2 = \frac{1}{R_R} + \frac{1}{R_M} + \frac{1}{R_F} + \frac{1}{r_F}; S_3 = \frac{1}{R_R} + \frac{1}{R_M} \tag{3}$$

2.2 Profiled ring geometry expansion prediction

As concerns the flange, its expansion is not controlled by any tool but is a free deformation caused by the lower plastic flow resistance toward its direction with respect to the circumferential direction (Fig. 1c,d). The material volume displaced by the movement of the mandrel toward the main roll, as well as the torque applied by the main roll itself, results in a circumferential expansion of the ring,

like in the flat ring rolling process, and a radial expansion of the flange, as shown in Fig. 2. By considering the volume conservation principle, and calculating first the deformation along the circumferential direction, the amount of material displaced from the wall to the flange can be estimated.

In all the equations relevant to the developed analytical model, the subscript “0” represents a parameter belonging to the initial ring geometry (preform), “i” for the i-round (current), and “i + 1” for the following round of the i-round process, respectively.

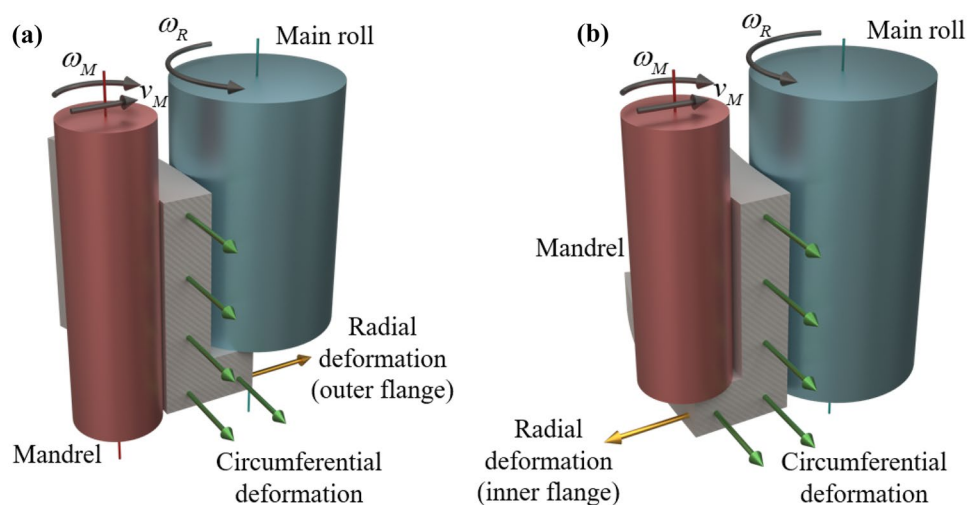
The first step for the proposed analytical model, Eq. (4), is the definition of the time required for a 360° rotation of a generic ring preform. The considered section is assumed to start its rotation when the mandrel starts its radial deformation. Equation (4) is derived for the first revolution, whereas Eq. (5) for the remaining rounds. Equation (5) is continuously updated for the whole mandrel time, allowing to calculate the time required for each revolution of the process based on the gear ratio between the main roll and the wall of the ring.

$$t_1 = \frac{2\pi R_{w,0}}{(\omega_R R_R)} \tag{4}$$

$$t_{i+1} = \frac{2\pi R_{w,i+1}}{(\omega_R R_R)} + t_i \tag{5}$$

Considering now the contact conditions between the tools and the wall part of the ring, the linearly decreasing mandrel

Fig. 2 Plastic deformation along the circumferential and radial (flange) directions, caused by the motions of the mandrel and the main roll, for **a** outer flange and **b** inner flange



feeding speed law, defined in [1] for the case of flat rings, Eq. (6), can be extended to the wall portion of profiled rings.

$$s_w(t) = s_{w,0} - \int_0^{t_j} v_M(t) dt = s_{w,0} - \left[\frac{v_{M,F} - v_{M,0}}{t_M} \frac{(t_j)^2}{2} + v_{M,0} \cdot t_j \right] \tag{6}$$

Accordingly, the variation of the ring wall thickness $s_w(t)$ is estimated at any process time included in the range $0 \leq t_j \leq t_M$, where t_M is the time during which the mandrel is active. For $t_j = 0$ the thickness of the ring is the same as the initial preform, $s_w(t) = s_{w,0}$, whereas for $t_j = t_M$ is that of the final ring, both considered as input variables in the analytical model. By considering a uniform evolution of the ring wall thickness between two consecutive revolutions, or rounds, of the process, for instance, the i - and the $i + 1$, the average thickness of the ring wall in the $i + 1$ revolution can be obtained by the integral of Eq. (6) in the time lapse $t_{i+1} - t_i$, as in Eq. (7). The definition of the ring thickness as “average” ($\bar{s}_{w,i+1}$) is given by the incremental nature of the ring rolling process where each circumferential section of the ring to have a different geometry in comparison to the previous one and the subsequent one.

$$\bar{s}_{w,i+1} = s_{w,0} - \frac{v_{M,0}}{2} (t_{i+1} - t_i) + \frac{v_{M,0} - v_{M,F}}{6t_M} \frac{t_{i+1}^3 - t_i^3}{t_{i+1} - t_i} \tag{7}$$

Considering the volume conservation principle and starting from an annular ring preform, the initial volume of the ring wall corresponds to the whole volume of the ring preform, Eq. (8), where $R_{w,0}$ and $R_{in,0}$ are the wall outer and inner radius of the ring preform, respectively. By updating the subscript of Eq. (8), the volume ring of the wall for the following revolutions, from the second to the last one, is calculated according to Eq. (9).

$$V_{w,0} = \pi (R_{w,0}^2 - R_{in,0}^2) (h_w + h_f) \tag{8}$$

$$V_{w,i} = \pi (R_{w,i}^2 - R_{in,i}^2) (h_w + h_f) \tag{9}$$

Concerning Eq. (8), if the initial ring preform is not flat but already flanged, it ought to be accounted for in Eq. (8) by considering only the volume relevant for the ring wall and not the whole volume of the initial preform. Moreover, in the developed analytical model, the height of both wall and flange are considered constants during the process. This assumption is reasonable because the axial rolls correct unwanted vertical deformations by spreading them along the radial direction [6] and for profiled rings, circumferential and radial (flange) expansions are normally the target parameters.

Hence, the volume variation of the ring wall $\Delta V_{w,i}$ is the volume reduction in the main roll-mandrel contact region as a function of the wall-flange height factor λ , Eq. (10). The λ factor accounts for the fact that a higher flange (h_f), in comparison to the wall height (h_w), increases the tendency of the material to move toward the circumferential direction instead of the radial one.

$$\Delta V_{w,i} = 2\pi \lambda h_f (\bar{s}_{w,i} - \bar{s}_{w,i+1}) \left(\bar{R}_{w,i} - [(\bar{s}_{w,i} - \bar{s}_{w,i+1})/2] \right) \tag{10}$$

where $\lambda = (\pi/2)h_f / (h_w + h_f)$

Having considered the volume variation of the ring wall during the i - revolution, the average radius of the ring wall, in the $i + 1$ round of the process ($\bar{R}_{w,i+1}$), is estimated by the combined application of Eqs. (6), (9) and (10), as shown in Eq. (11). The main geometrical variable estimated by the proposed analytical model and the relevance for both wall and flange are summarized in Fig. 3.

$$\bar{R}_{w,i+1} = \frac{[V_{w,i} - \Delta V_{w,i}]}{2\pi \bar{s}_{w,i+1} (h_w + h_f)} \tag{11}$$

In Fig. 3, the average radius of the ring wall ($\bar{R}_{w,c}$) is indicated in the middle of the ring wall cross-section, but, in general, it refers to the spatial averaging, across 360°, of the radius starting from the ring center and ending at the center of the wall cross-section. Once the average radius of the ring wall in the $i + 1$ revolution is calculated, the inner and outer radii of the ring wall are derived by subtracting and adding half of the wall thickness, Eq. (7), resulting in Eq. (12).

$$R_{in,i+1} = \bar{R}_{w,i+1} - \frac{\bar{s}_{w,i+1}}{2}, R_{w,i+1} = \bar{R}_{w,i+1} + \frac{\bar{s}_{w,i+1}}{2} \tag{12}$$

According to the volume conservation principle, the ring wall volume variation in the $i + 1$ revolution is considered to move from the wall to the flange, allowing to

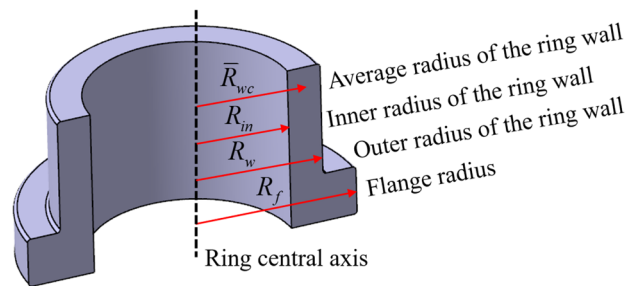


Fig. 3 Flanged ring radii identification on a generic ring cross-section

estimate of the flange radius in the $i + 1$ revolution as in Eq. (13).

$$R_{f,i+1} = \sqrt{\frac{V_{w,0} - V_{w,i+1}}{\pi h_f} + R_{w,i+1}^2} \tag{13}$$

Finally, if the process is considered to start from an annular preform, the initial flange diameter, $R_{f,0}$, is equal to the initial outer radius of the wall $R_{w,0}$. However, if the process starts from a non-annular preform, the initial radius of the flange must be added to $R_{f,i+1}$ and becomes a constant.

3 Finite element model and validation cases settings

To validate the analytical model described in the previous section and further investigate the material distribution in the cross-section of profiled rings, a thermo-mechanical FEM model has been implemented and validated considering the literature and previous authors’ experimental results. The details are reported in Sect. 3.1. Additional FEM models have also been developed to perform a comparison of authors’ analytical predictions with literature experimental and FEM results. Four validation cases have been considered, and the relevant details are summarized in Sect. 3.2.

3.1 Finite element model details

The thermo-mechanical FEM simulations have been implemented in the commercial SW Simufact Forming 16. The mesh for the ring geometries has been defined considering a 3D arbitrarily distorted 8-node, first-order isoparametric (MARC® element type 7) formulation, well suited for contact analysis, such as for the case of the ring rolling process and by employing the “ring mesh” tool available in Simufact Forming. To accurately describe the stress gradient throughout the element, the Newton/Cotes/Lobatto solution scheme

has been adopted and allowed considering the integration points in the middle position between the edges and in the centroid of the element.

The tools have been considered as rigid with heat transfer and meshed with the 3D 8-node, first-order isoparametric heat transfer element (MARC® element type 43). A representation of the implemented FEM model is shown in Fig. 4, where the axial rolls, originally positioned as in Fig. 1a, have been removed to allow a better view of the ring-tools contact region.

For each one of the implemented cases, defined as a set of ring rolling mill tools and a ring geometry, four different mesh strategies have been tested, allowing us to conclude that the best compromise between accuracy and computational time is represented by (i) 1 element every 1° for the circumferential direction, (ii) 1 element every 2.5 mm for the radial direction, and (iii) 1 element every 2.5 mm for the vertical direction. For the solution, the MULTifrontal Massively Parallel sparse direct Solver (MUMPS) direct solver has been employed along with the updated Lagrangian approach for the estimation of the node displacement. Both solver and node displacement calculations are well suited for large deformations, such as the case of circumferential and flange growths in the profiled ring rolling.

Friction has been modeled considering the shear friction law of Eq. (14), where the yield strength (k) is calculated according to the von Mises criterion. In the implemented FEM simulations, a friction factor $m = 0.85$ has been utilized for the contact between the main roll and mandrel with the ring and $m = 0.6$ for the contact between axial rolls and guide rolls with the ring. The two friction factors have been defined considering the ranges made available by Sun et al. [55] and already employed in previous authors’ contributions [1, 6–8]. The higher friction factor considered for the mandrel-main roll contact with the ring is motivated by the higher pressure, and relevant thickness draft, applied by these two tools to the rings, in comparison to the axial rolls.

Fig. 4 Thermo-mechanical finite element simulation model implementation

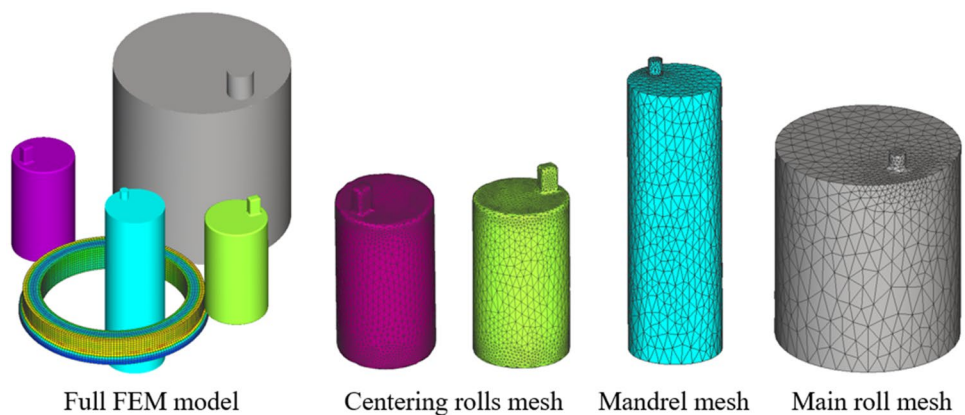


Table 1 Material constants and validity range for the Inconel 718 and 42CrMo4 (Hensel-Spittel flow stress model)

Parameter	Inconel 718	42CrMo4
Temperature range for the model [°C]	950~1100	800~1250
Strain range for the model [-]	0.05~2	0.05~2
Strain rate range for the model [1/s]	0.01~150	0.01~150
C_1	10,501.1	5290.5
C_2	-0.0030755	-0.0036967
n_1	-0.0001815	-0.0003340
n_2	0.543976	0.206120
L_1	-2.17606e-5	-8.26584e-5
L_2	0.0237644	0.0289085
m_1	-2.67316e-6	0.0003007
m_2	0.0974653	-0.1561810

$$\tau = m \cdot k \tag{14}$$

The heat transfer coefficients for conduction and convection have been set to 5000 W/(m²·K) and 50·W/(m²·K), whereas the emissivity, relevant for the radiation heat transfer, has been set to 0.7. The temperature-dependent Young’s moduli, thermal conductivity, and specific heat capacity properties, for both materials, are reported in Appendix 1 (Figs. 13 and 14). The tools have been set with an initial temperature equal to 150 °C, whereas the ring with an initial temperature equal to 1030 °C for the Inconel 718 rings and 1200 °C for the 42CrMo4 rings, respectively.

In terms of materials, a nickel-based Inconel 718 and a 42CrMo4 steel alloy have been considered being both largely utilized in the ring rolling process [41, 56–60]. The material properties have been acquired from the MATILDA® (Material Information Link and Database Service) database available in Simufact Forming 16. The strain, strain rate,

and temperature-dependent plastic behaviors of both alloys have been modeled by the Hensel-Spittel flow stress equation [61], Eq. (15), and the relevant model constants are reported in Table 1.

$$\sigma = C_1 e^{(C_2 \cdot T)} \epsilon^{(n_1 \cdot T + n_2)} e^{\left(\frac{L_1 \cdot T + L_2}{\epsilon}\right)} \dot{\epsilon}^{(m_1 \cdot T + m_2)} \tag{15}$$

By means of the implemented finite element model, two different investigations have been carried out to validate the proposed analytical model as well as to better understand the correlation between process settings and geometrical expansion in the profiled ring rolling process.

The former investigation aimed at understanding the role played by the process parameters, in terms of main roll rotation speed and mandrel initial-final feedings speeds, on the material redistribution in the cross-section of profiled rings. To this aim, three different initial and final ring configurations have been coupled with three different main roll rotational speeds. For each main roll rotational speed, three initial and final mandrel feeding speed sets have been calculated at the extreme points and in the middle of the ranges defined in Eqs. (1)–(3), for a total of 27 cases implemented considering the Inconel 718 alloy. A summary of the key parameters of the process settings influence investigation is reported in Table 2, whereas the remaining input values are reported in Appendix 2.

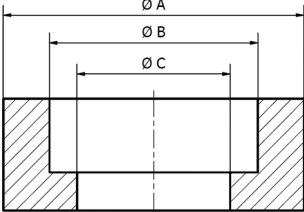
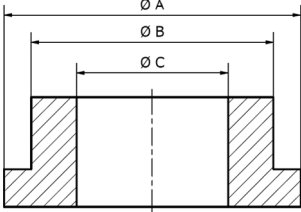
To account for the simultaneous variation of both main roll rotation speed and mandrel feeding speeds, the velocity parameter (v) reported in Eq. (16) has been defined and utilized for the plot of the results relevant to the process settings influence investigation, reported in Sect. 4.2.

$$v = \frac{([v_M]_0 + [v_M]_F)}{2\omega_R} \left[\frac{mm/s}{rad/s} \right] \tag{16}$$

Table 2 Process and geometrical parameters for the process settings influence investigation

Parameters	Ring#1A	Ring#2A	Ring#3A
Main-roll radius [mm]	270	375	490
Mandrel radius [mm]	90	125	165
Initial ring outer diameter [mm]	235	325	425
Initial ring wall thickness [mm]	90	120	160
Initial ring height [mm]	145	145	145
Final ring wall thickness [mm]	54	72	96
Final ring flange thickness [mm]	72	96	128
Final ring outer flange diameter [mm]	564	802	1011
Final ring outer wall diameter [mm]	528	754	947
Final ring internal diameter [mm]	420	610	755
Main roll rotational speed range [rad/s]	$2 \leq \omega_R \leq 4$		
Mandrel feeding speed range [mm/s]	$0.16 \leq v_M \leq 6.84$	$0.2 \leq v_M \leq 9.7$	$0.28 \leq v_M \leq 12.59$
Mandrel active time range [s]	$5.26 \leq t_M \leq 139$	$5.05 \leq t_M \leq 140$	$5.08 \leq t_M \leq 139.5$

Table 4 Ring rolling mill dimensions, initial and final ring geometries, and process settings for the internal and external L-shape rings validation cases [46, 48]

Parameters	Internal flange [46]	External flange [48]
Main-roll radius [mm]	100	100
Mandrel radius [mm]	45	45
Initial ring outer diameter [mm]	196	222.6
Initial ring wall thickness [mm]	41.5	40.1
Initial ring flange thickness [mm]	41.5	40.1
Initial ring height [mm]	40.8	44.4
Final ring wall thickness [mm]	15.1	15
Final ring flange thickness [mm]	30.2	18
Final ring wall height [mm]	17.55	26.4
Final ring flange height [mm]	23.25	18
Diameter A [mm]	270	396
Diameter B [mm]	239.8	376
Diameter C [mm]	209.6	346
Thickness reduction per rev. [%]	4	1
Final shape schematic reference		

The same input parameters summarized in Table 2 and Appendix 2 have also been utilized as inputs for the developed analytical model for the prediction of the

geometrical expansion of the 27 cases, subsequently compared with the FEM results to assess the relevant prediction accuracy.

Table 3 Ring rolling mill dimensions, initial and final ring geometries, and process settings for the plastic flow investigation

Parameters	Ring #1B	Ring #2B	Ring #3B	Ring #4B	Ring #5B	Ring #6B	Ring #7B	Ring #8B	Ring #9B
Main-roll radius [mm]	270			375			490		
Mandrel radius [mm]	90			125			165		
Wall thickness reduction [%]	70%	60%	50%	70%	60%	50%	70%	60%	50%
Flange protrusion from initial wall thickness [%]	10%	20%	30%	10%	20%	30%	10%	20%	30%
Initial ring outer diameter [mm]	235			325			425		
Initial ring wall thickness [mm]	90			120			160		
Initial ring height [mm]	145			145			145		
Final ring flange thickness [mm]	72			96			128		
Final ring wall thickness [mm]	63	54	45	84	72	60	112	96	80
Final ring outer flange diameter [mm]	519	564	619	712	802	852	926	1011	1106
Final ring outer wall diameter [mm]	501	528	565	688	754	780	894	947	1010
Final ring internal diameter [mm]	375	420	475	520	610	660	670	755	850
Final ring flange height [mm]	50								
Final ring wall height [mm]	95								
Main-roll rotational speed [rad/s]	4								
Initial mandrel feeding speed [mm/s]	6.88	6.84	6.79	9.8	9.7	9.72	12.67	12.6	12.52
Final mandrel feeding speed [mm/s]	6.82	6.54	6.16	9.6	8.9	8.67	12.6	12.05	11.38
Mandrel active time [s]	3.92	5.26	6.63	3.67	5.05	6.17	3.79	5.08	6.39
Total process time [s]	5	6.5	8	5	6.5	7.5	4.5	6.5	8

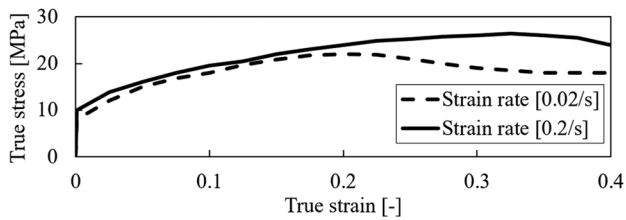


Fig. 5 True stress–strain curves at 0.2/s and 0.02/s for the BS EN 12,588 lead alloy [46]

The latter analysis, defined as plastic flow investigation, aims to provide an insight into the performances of the analytical model when the same initial ring shape is considered as the preform for the manufacturing of different final shapes with different wall-to-flange thickness ratios.

In this second analysis, different sets of initial and final mandrel feeding speeds have been calculated according to Eqs. (1)–(3) to control the volume of the material flowing from the wall to the flange of the ring. To avoid any influence of the main roll rotation speeds, in all the nine cases of the plastic flow investigation, Table 3, the same main roll rotational speed, equal to 4 rad/s, has been utilized.

3.2 Validation cases

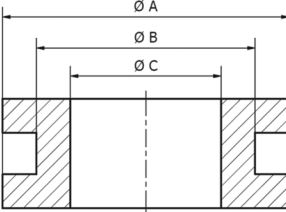
To validate the analytical model with different profiled ring geometries, experimental and FEM results relevant to four literature contributions have been considered and are summarized in this section.

3.2.1 Internal and external L-shape flange (flat ring preform)

For the internal L-shape flange [46], the literature FEM results concerning the radial forming force and the experimental one relevant for the geometrical expansion of the ring have been compared with the analytical and FEM predictions calculated by the authors. For the external L-shape flange [48], the experimental results relevant to the geometrical expansion of the ring have been compared with both analytical and FEM authors' calculations. The ring rolling mill, initial, and final ring dimensions for internal and external L-shape flanges validation cases [46, 48] are reported in Table 4.

For the FEM simulation development, the same meshing strategy and solver, as described in Sect. 3.1, have been adopted. To match the boundary conditions summarized in [46, 48], friction has been modeled with a Coulomb law and a friction coefficient equal to 0.15, whereas environment and tools temperatures have been set to 20 °C. In both cases, the BS EN 12,588 lead alloy, Fig. 5 [46], was utilized and the literature plastic properties have been inputted in the FEM simulations.

Table 5 Ring rolling mill dimensions, initial and final ring geometries, and process settings for the C-shape validation cases [53]

Parameters	Value
Main-roll radius [mm]	570
Mandrel radius [mm]	150
Guide rolls radius [mm]	150
Initial ring temperature [°C]	1000
Tools temperature [°C]	150
Friction coefficient	0.3
Initial ring outer diameter [mm]	756.4
Initial ring inner diameter [mm]	456.4
Initial ring height [mm]	223.1
Final ring wall thickness [mm]	60.8
Final ring flange thickness [mm]	101.5
Final ring wall height [mm]	82.5
Final ring total height [mm]	223.1
Diameter A [mm]	1164.3
Diameter B [mm]	1082.9
Diameter C [mm]	961.3
Main-roll rotational speed [rad/s]	1.1
Mandrel feeding speed [mm/s]	0.3
Final shape schematic reference	

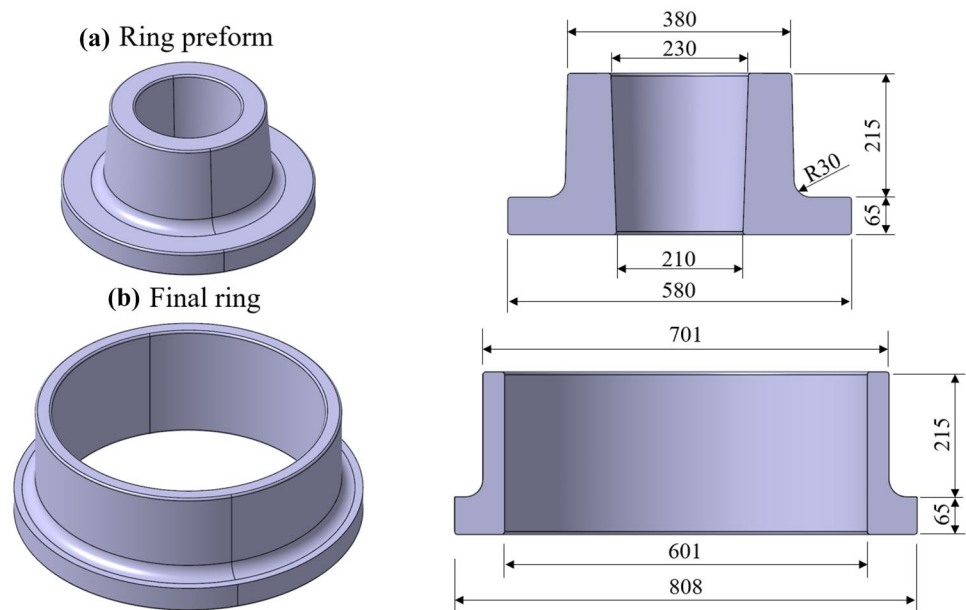
3.2.2 External C-shape flange (flat ring preform)

As concerns the double L-shape (C-shape) geometry, the experimental case presented in Liang et al. [53] and manufactured with the Inconel 718 superalloy has been considered. In the FEM modeling for this case, the same material properties and flow stress modeling reported in Eq. (15) and Table 1 have been utilized. Ring rolling mill geometry, ring initial and final dimensions, and process conditions for this validation case [53] are reported in Table 5.

3.2.3 External L-shape flange (flanged ring preform)

To validate the applicability of the proposed analytical model also for the case of a non-annular ring preform, the experimental results relevant to one of the authors' previous contributions [41] have been utilized. The initial (preform) and final profiled ring shapes are reported in Fig. 6a, b, respectively. The ring material is the 42CrMo4 alloy and the relevant model and constants, utilized for the setting of the FEM simulation, are those previously summarized in Eq. (15) and Table 1.

Fig. 6 **a** Initial and **b** final geometry of the authors' validation case (Monti and Berti [41])



The ring rolling mill dimensions and the process settings employed in both the real production and implemented in the FEM model are reported in Table 6. Since the material, process conditions, finite element program, and solution scheme are almost identical to those utilized in the development of the FEM model employed in this research, these experimental results are particularly useful for a concurrent validation of both analytical and finite element models.

4 Results and discussion

In this chapter, the results relevant for validating the proposed analytical model and the implemented finite element simulation are summarized case by case in Sect. 4.1, following the order defined in Sect. 3.2. Afterward, the results and considerations relevant to the process settings influence

Table 6 Ring rolling mill dimensions, initial and final ring geometries, and process settings for the external L-shape and non-annular preform case [41]

Parameters	Value
Main-roll radius [mm]	100
Mandrel radius [mm]	50
Guide rolls radius [mm]	75
Initial ring temperature [°C]	1240
Initial tools temperature [°C]	400
Friction coefficient	0.15
Main-roll rotational speed [rad/s]	6.28
Initial ~ final mandrel feeding speed [mm/s]	1 ~ 0.58

and plastic flow investigations are reported in Sects. 4.2 and 4.3, respectively.

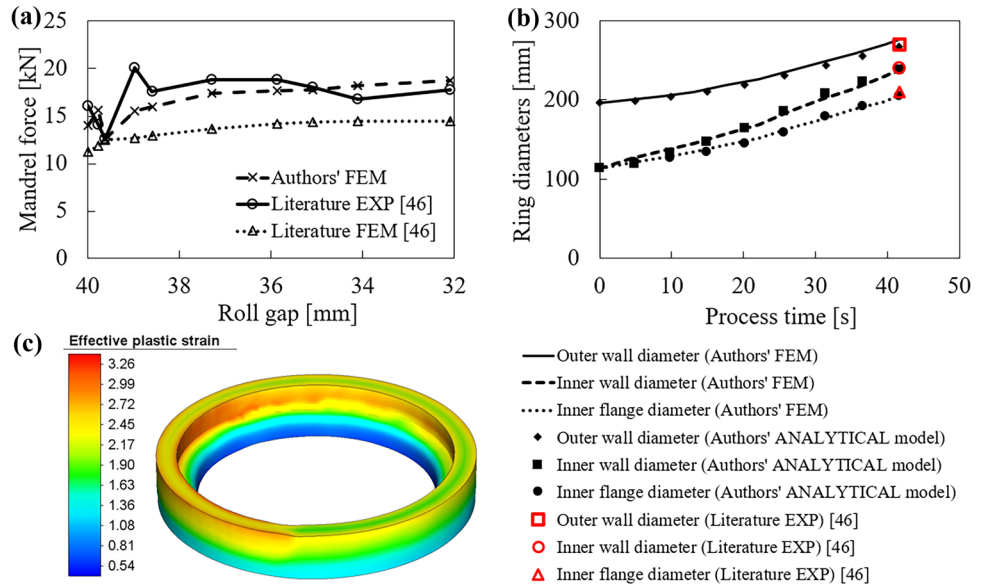
4.1 Analytical and FEM model validation results

As concerns the internal L-shape flange, the first analysis is devoted to the comparison among literature experimental and FEM mandrel forming force results [46] and the authors' FEM solution, implemented considering the same material properties, process conditions, and ring and tools geometries.

Taking as reference the literature experimental results, the maximum and average deviations, with respect to the authors' FEM solution, are estimated at 12.5% and 6.8%, respectively (Fig. 7a), except for the sudden peak around 39 mm of the roll gap, most likely caused by the collision between the ring and one of the centering rolls, a frequent issue in the first stages of the ring rolling. The higher similarity between authors' FEM results and literature experiment, in terms of mandrel forming force (Fig. 7a), has been attributed to the ring rolling simulation tool available in Simufact Forming, which allows for a more realistic setting and estimation of the tool's motion, and to the ring mesher toolbox, specifically designed to create an accurate mesh and perform in-simulation remeshing of ring-shaped components.

In Fig. 7b, the authors' analytical and FEM model results are compared with the experimental value [46] of the final geometry of the ring at the end of the expansion phase. The deviations, in terms of wall and flange diameters, are equal to 1.05% for the ring outer wall, 1.2% for the ring inner

Fig. 7 Authors' FEM and analytical model validation for inner L-shape flange. **a** Comparison between authors' FEM simulation and literature [46] experimental and FEM results for the mandrel forming force. **b** Comparison between FEM simulation, analytical model prediction, and literature [46] experimental results for the round-based diameters growth. **c** Effective plastic strain distribution from the authors' FEM simulation replicating the literature [46] case at the end of the ring expansion phase



wall, and 2.5% for the inner flange. The results of Fig. 7b show good agreement between the authors' analytical and FEM solutions, throughout the process. It is also interesting to remark that, by inputting the same initial and final ring geometries and applying the same process parameters of [46], the authors' analytical model can predict the final shape of the ring obtained from the literature experiment with reasonable accuracy. The final ring, at the end of the calibration phase, estimated by means of the authors' FEM model, is reported in Fig. 7c. In addition, the good agreement between the authors' FEM and experimental mandrel force, Fig. 7a, allows inferring that the implemented FEM

simulation is reliable in replicating the deformation behavior throughout the whole process.

Regarding the outer flange profiled ring [48], the comparison between the authors' analytical and FEM solutions with the literature experimental results are reported in Fig. 8 in terms of roll gap, defined as the distance between the mandrel and the main roll or, in other words, the thickness of the ring wall. For the case of the outer L-shape flange of [48], being available the evolution of the three main ring diameters at certain instants during the process, they can be compared to the continuous-like results provided by the authors' analytical model and FEM simulation.

Fig. 8 Authors' FEM and analytical model validation for outer L-shape flange. Comparison between authors' FEM simulation, analytical model, and literature [48] experimental results for the **a** ring outer flange diameter, **b** ring outer wall diameter, and **c** ring inner wall diameter. **d** Effective plastic strain distribution from the authors' FEM simulation replicating [48] case at the end of the ring expansion phase

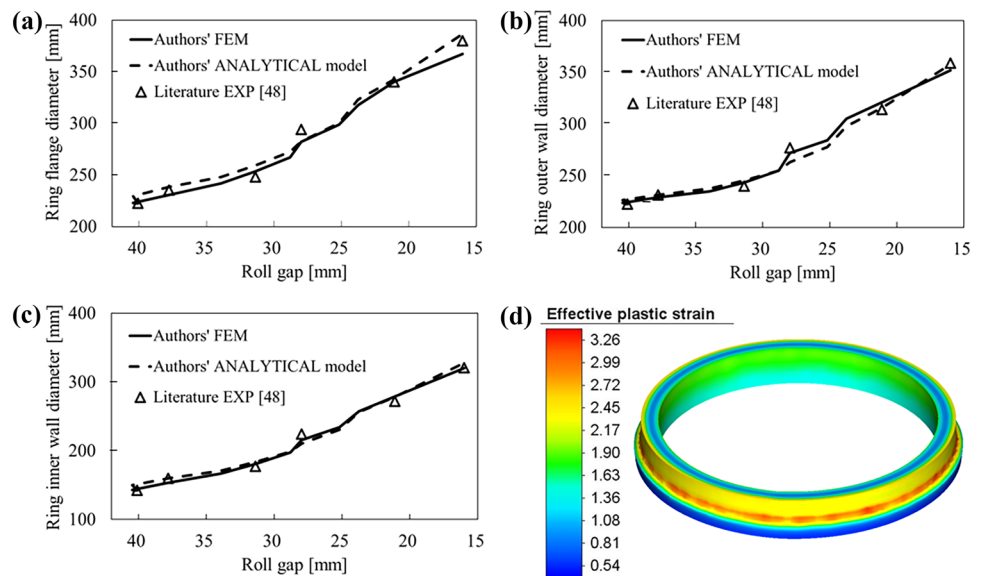
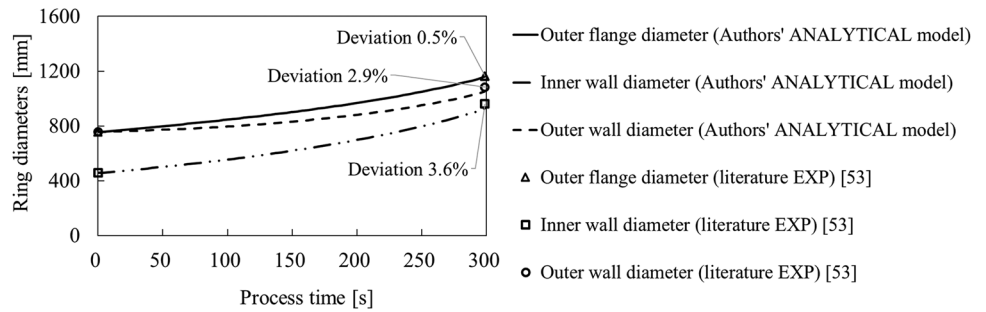


Fig. 9 Authors’ analytical model validation for outer C-shape flange in terms of comparison with the literature experimental results for the outer flange diameter, inner wall diameter, and outer wall diameter with respect to the process time



As shown in Fig. 8a–c, the authors’ analytical model accurately estimates the final geometry of the ring, and at the same time, it catches the trend of the geometrical expansion, in comparison to both FEM and experimental results. For the case of the external L-shape flange ring, the maximum and average deviations between the authors’ analytical model and literature experimental results are quantified at 4.5% and 1.1% for the outer flange diameter, 6.4% and 1.4% for the inner wall diameter, and 5.1% and 0.75% for the outer wall diameter, respectively. Also, for this second validation case, the authors’ FEM and analytical solutions well agree both with the final values at the end of the process time (minimum value of the roll gap) and during the ring expansion phase.

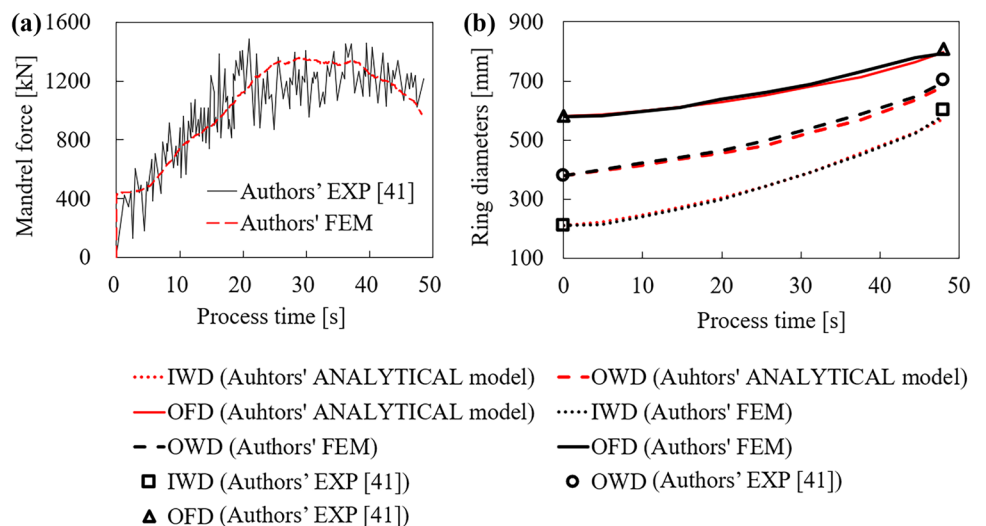
Considering the third literature validation case, the authors’ analytical model predictions have been compared with the experimental results of Liang et al. [53], available in terms of the initial and final geometry of a C-shape outer flanged ring, Table 5. The considered geometry is symmetric along the horizontal direction; thus, the upper and the lower flange expansions are considered to be equal. In the results

comparison presented in Fig. 9, the deviations between the authors’ analytical model and the literature experimental results are calculated on the ring final diameters and are equal to 0.5% for the outer flange, 3.6% for the inner wall, and 2.9% for the outer wall, respectively.

The last validation presented in this section of the paper aims to provide an insight into the capability of the developed analytical model of accurately predicting the geometrical expansion of profiled rings also for the case of an already-profiled ring preform. The settings are those in Fig. 6 and Table 6.

To further validate the developed FEM model, the first result, reported in Fig. 10a, shows a comparison between experimental and FEM signals for the mandrel feeding force. The former data has been directly extracted from the ring rolling machine during the process. The consideration of a flanged preform leads to a slightly more unstable process, testified by the sudden variation of the radial forming force from the very beginning of the FEM simulation. On the other hand, for the case of the experimental results, the localized variations during the whole processing time are

Fig. 10 a Comparison between authors’ FEM and experimental [41] results for the mandrel force. **b** Comparison of FEM, analytical, and experimental results for the expansion of the inner wall diameter (IWD), outer wall diameter (OWD), and outer flange diameter (OFD) with respect to the process time



caused by several factors, among them the presence of oxidation scale forming and detaching from the ring surface and the variation of the lubrication conditions during the process. Although all these factors contribute to some degree of instability, the FEM result follows well the trend of the experimental force, being almost in between the local maximum and minimum values of the raw signal. The average deviation of the two results reported in Fig. 10a, estimated at 14.8%, has been calculated as the average ratio between experimental and FEM results on 20 points between 0 and 48 s (final time).

As concerns the estimation of the geometrical expansion of the ring, the analysis of the results reported in Fig. 10b shows good agreement among experimental, FEM, and analytical results, proving the capability of the proposed analytical model to well describe the material redistribution in profiled rings, even for the case of starting from a non-annular preform. The deviations, calculated at the end of the expansion phase of the process, are summarized in Table 7, where IWD is the inner wall diameter, OWD is the outer wall diameter, and OFD is the outer flange diameter, respectively.

It must be highlighted that the consistency between the analytical model and FEM solutions shows that the proposed analytical model can be utilized as an initial screening phase to investigate the influence of process and geometrical parameters on the expansion of the ring, relying on FEM simulations only in a further step. This double analytical-FEM approach allows saving precious time since the initial calculations are straightforward and carried out in real-time.

Considering the results presented in this subsection, relevant for a wide range of profiled ring geometries, materials, and process settings, it is fair to say that the implemented FEM simulation is capable of properly replicating the profiled ring rolling process. Therefore, in the following two sub-sections, the validated FEM model is utilized, in combination with the developed analytical model, for the investigation of the influence of the process parameters on the geometrical expansion and material redistribution in the cross-section and circumferential direction of profiled rings.

4.2 Process settings influence investigation results

For the case of the profiled ring rolling, the process settings have shown a great deal of influence on the material redistribution from the ring wall toward both circumferential and radial directions, thus on the correct expansion of the flange. The plastic flow resistance is directly influenced by the material yield strength, a fact that links these two parameters to the capability of the analytical model in accurately predicting the geometrical expansion of profiled rings. To this aim, the influence of the process parameters, in terms of main roll rotational speed and relevant initial and final mandrel feeding speeds, on the accuracy of the geometrical prediction carried out by the developed analytical model has been investigated considering 27 cases and the Inconel 718 alloy material, Fig. 11a. The FEM simulation settings relevant for this investigation are summarized in Table 2 and Appendix 2 of the paper. The y-axis of Fig. 11a represents the maximum difference between FEM and analytical model results, in terms of prediction of the inner wall diameter, the outer wall diameter, and the flange diameter, measured at 20%, 40%, 60%, 80%, and 100% of the mandrel time. Due to the slightly curved shape of the flange in the FEM simulations, the flange diameter is defined as the average between the smaller values at the top of the flange and the larger ones at its bottom.

Considering the results of Fig. 11a, a discontinuity in the analytical model prediction accuracy is clearly identified. If the process is carried out at a relatively high main roll rotational speed and mandrel feeding speeds, thus for a high-velocity parameter (v), the temperature drop in the ring during the process is relatively low and the analytical model accuracy is comparable to that of FEM simulations, reaching a drop to a 6.1% maximum deviation from a velocity parameter close to 1.

On the other hand, if the velocity parameter becomes lower than 1, the maximum deviation almost doubles and reaches a peak at 11.6% for $v = 0.137$, representing a point where the main roll rotational speed is relatively high (4 rad/s) but where initial and final mandrel feeding speeds are relatively low and equal to 0.7 mm/s and 0.4 mm/s,

Table 7 Experimental, FEM, and analytical results comparison for the L-shape profiled ring (flanged ring preform) in terms of final ring geometry

Value	IWD [mm]	OWD [mm]	OFD [mm]
Experiment (Monti and Berti [41])	601	701	808
Authors' FEM	581.8	693.4	792.4
Authors' analytical model	571.7	681.7	796.1
EXP vs authors' FEM deviation	3.2%	1.1%	1.9%
EXP vs Authors' analytical model deviation	4.9%	2.8%	1.5%

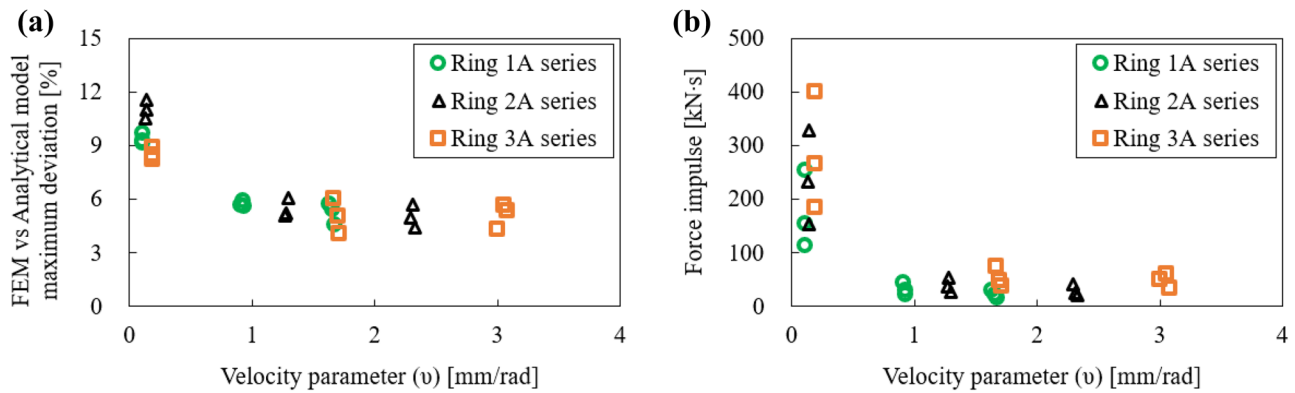


Fig. 11 Influence of the main roll rotational speed and initial and final mandrel feeding speeds on the accuracy of the analytical model and on the force integral of mandrel active time

respectively. It is interesting to highlight that, for the case of the same Ring 2A series, the same main roll rotational speed of 4 rad/s, combined with two higher initial and final mandrel feeding speeds of 9.7 mm/s and 8.9 mm/s, leads to a considerably lower deviation of 4.4%. The same trend is also experienced by Ring 1A and Ring 3A series, as shown in Fig. 11a.

Considering this variation of the analytical model accuracy with respect to the velocity parameter, some aspects relevant to the ring rolling process should be clarified for a better understanding of their implications on the range of applicability of the proposed analytical model. In both flat and profiled ring rolling processes, huge variations of the ring temperature between the beginning and the end of the process lead to uneven microstructure evolution and an increase in the forming force. This fact is visible in the results reported in Fig. 11b, where the force impulse relevant for the same 27 cases is plotted against the velocity parameter. The cases where the analytical model has the highest deviations are also those where the forming force is the highest and where the velocity parameter is the lowest. On top of that, a relatively long process time induces a large oxidation scale formation on the ring surface, which inevitably affects the dimensional accuracy.

For these reasons, the proposed analytical model is well suited for the application in the hot ring rolling process since the temperature drop will not be high enough to influence the overall accuracy of the geometrical prediction. Moreover, considering the real-time estimation of the ring geometrical expansion carried out by the proposed algorithm, in comparison to the FEM solution where the average computational time is about 18 h, the improvement is remarkable.

4.3 Plastic flow investigation results

As concerns the second investigation, three initial ring preforms have been utilized for the realization of three final rings each, as summarized in Table 3. By controlling the process parameters, the plastic flow from the preform wall to the circumferential and radial (flange) directions has been investigated to analyze the capability of the proposed analytical model to account for the material redistribution if different process parameters are applied to the same initial ring geometry.

The same geometry and process conditions have been applied to the Inconel718 and 42CrMo4 materials to show the kinematic nature of the geometrical expansion of profiled rings, defined as one of the key assumptions for the analytical model. As previously mentioned, this statement is true if the temperature drop between the beginning to the end of the process is not high enough to cause a significant change in the flow stress of the material.

Also, for the case of the plastic flow investigation, the accuracy in the estimation of the ring geometry has been carried out by comparing the results of the FEM simulation with those of the proposed analytical model at 20%, 40%, 60%, 80%, and 100% of the mandrel time. The results for the nine cases and two materials considered in this analysis are summarized in Table 8 and show maximum and average deviations equal to 6.05% and 1.94%, respectively.

Considering the results of Table 8, the deviations between analytical model predictions and FEM results are remarkably similar for both materials, being 2.15% (average) and 6.05% (maximum) for the Inconel 718 and 1.74% (average) and 5.42% (maximum) for the 42CrMo4,

Table 8 Analytical vs FEM deviations for the plastic flow investigation for Inconel 718 and 42CrMo4 materials under the same initial/final geometries and process conditions

Material	Geometrical parameters	Percentage of the total process time [%]									
		Inconel 718					42CrMo4				
		20%	40%	60%	80%	100%	20%	40%	60%	80%	100%
Ring #1B	Inner wall diam. [mm]	2.73	1.19	3.45	2.95	1.26	2.17	0.77	2.91	0.79	0.08
	Outer wall diam. [mm]	1.85	0.61	2.74	2.00	1.70	2.03	0.82	0.25	0.34	1.36
	Flange diam. [mm]	1.67	1.04	3.96	3.87	1.06	2.47	2.53	1.76	3.71	0.96
Ring #2B	Inner wall diam. [mm]	2.17	1.28	2.29	1.29	1.02	0.25	3.06	0.57	1.42	2.71
	Outer wall diam. [mm]	0.78	1.16	3.54	2.83	0.56	1.49	0.86	2.55	3.44	4.31
	Flange diam. [mm]	0.61	2.02	2.50	0.93	3.26	1.33	0.54	2.04	1.32	0.21
Ring #3B	Inner wall diam. [mm]	2.63	1.15	3.27	2.26	1.71	1.67	0.91	2.69	1.70	1.38
	Outer wall diam. [mm]	0.24	1.28	1.63	2.31	3.46	1.14	1.24	4.03	1.74	0.89
	Flange diam. [mm]	0.95	1.67	1.94	1.60	4.34	2.06	0.66	0.82	0.96	4.29
Ring #4B	Inner wall diam. [mm]	2.82	2.32	1.68	0.93	0.51	2.97	1.84	0.64	1.13	1.63
	Outer wall diam. [mm]	1.72	0.83	1.51	1.26	2.04	0.05	0.17	0.62	1.14	0.63
	Flange diam. [mm]	2.03	4.06	3.08	2.59	0.37	2.57	2.11	3.05	3.39	0.28
Ring #5B	Inner wall diam. [mm]	1.50	2.06	1.06	0.45	2.34	1.05	2.07	0.10	0.28	1.62
	Outer wall diam. [mm]	0.13	0.13	0.82	1.16	0.65	0.80	1.59	0.60	1.40	0.65
	Flange diam. [mm]	1.80	2.19	2.11	2.20	3.70	1.07	2.65	3.05	2.74	3.69
Ring #6B	Inner wall diam. [mm]	0.07	1.54	4.39	6.05	3.23	1.02	0.86	3.01	5.41	3.45
	Outer wall diam. [mm]	0.49	0.10	2.75	4.28	0.97	0.09	0.39	0.17	1.91	2.20
	Flange diam. [mm]	1.54	0.68	0.28	1.09	5.34	1.08	1.26	0.16	1.18	4.73
Ring #7B	Inner wall diam. [mm]	1.93	3.19	4.98	3.09	3.05	1.90	3.52	5.42	3.33	3.42
	Outer wall diam. [mm]	0.57	1.69	3.00	0.91	0.19	1.95	2.35	2.29	0.40	0.74
	Flange diam. [mm]	1.73	4.63	5.40	4.15	4.66	2.40	3.34	4.81	4.28	4.00
Ring #8B	Inner wall diam. [mm]	3.73	4.06	2.77	0.28	3.85	0.98	1.62	0.98	1.94	1.03
	Outer wall diam. [mm]	0.01	2.62	4.60	3.54	3.99	1.63	0.12	0.33	0.61	0.70
	Flange diam. [mm]	0.23	3.31	3.15	4.01	2.61	0.85	0.82	0.68	1.20	3.04
Ring #9B	Inner wall diam. [mm]	2.89	3.33	1.14	0.75	1.71	2.40	3.93	0.09	0.00	0.12
	Outer wall diam. [mm]	2.86	1.70	0.54	1.24	0.54	0.73	1.85	0.54	0.97	0.92
	Flange diam. [mm]	3.19	4.49	3.09	2.02	1.07	2.64	4.91	2.84	2.64	1.40

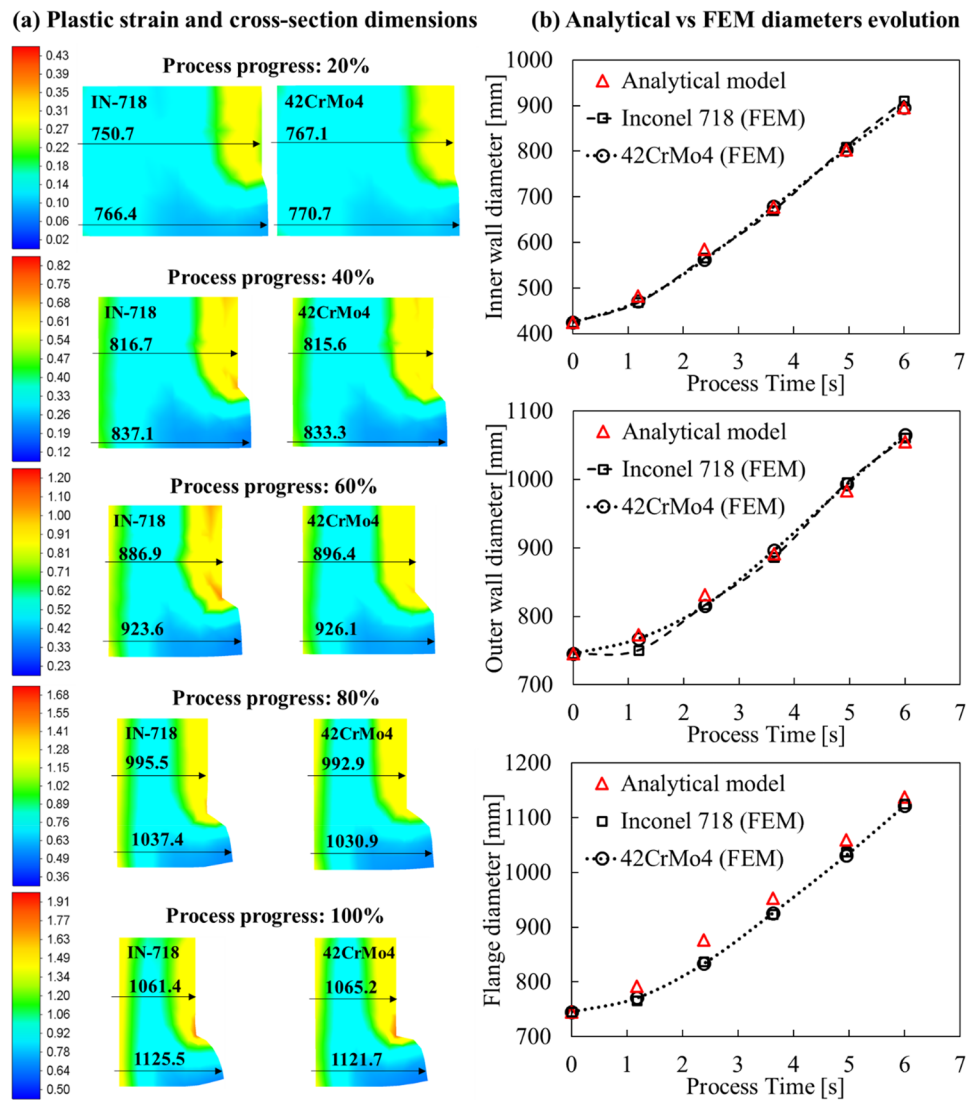
respectively. Since the proposed analytical model is fully kinematic, its predictions for both Inconel 718 and 42CrMo4 materials are identical but have been compared with fully thermo-mechanical FEM models implemented considering the strain, strain rate, and temperature influences on the flow stress.

The uniformity of the deviations, despite the differences in the flow stress behavior, shows that the geometrical expansion is mostly controlled by the kinematic movement of the tools and the friction conditions, a fact that makes the proposed analytical solution to have good, and similar, accuracies in both cases. As additional proof to this statement, the equivalent plastic strain distribution in the cross-section of the Ring #9B of Table 8, exported at 20%, 40%, 60%, 80%, and 100% of the mandrel time, and relevant for the Inconel 718 and 42CrMo4 materials, has been summarized in Fig. 12a along with the process

time-dependent evolution of the main three ring diameters, Fig. 12b.

Overall, the result comparison proposed in Fig. 12 confirms that the proposed analytical model can also be applied to materials and process conditions different from those utilized in this research, and it proves the generality of the proposed solution and the validity of the adopted kinematic assumption. Considering altogether the results summarized in this section of the paper, the developed analytical model showed its applicability to a large variety of profiled rings, from L-shape to C-shape, and also for the case of non-annular ring preform. Besides, the real-time estimation provided by the proposed solution is one of the main strength points of the analytical solution that showed an accuracy comparable to FEM simulations if the ring rolling process is carried out, avoiding too high-temperature losses.

Fig. 12 **a** Equivalent plastic strain and geometrical expansion comparison between Inconel 718 and 42CrMo4 materials and **b** main diameters expansion throughout the process (analytical VS FEM)



5 Conclusions

In this research, an analytical model estimating the geometrical expansion of profiled rings in the ring rolling process was presented and validated against literature experimental and FEM results for internal and external L-shapes and C-shape rings. Also, the influence of the ring preform and the process parameters on the material redistribution in the cross-section and the prediction accuracy of the proposed model has been investigated in terms of geometrical expansion of the ring. Within the wide range of geometry and process parameters considered in this research, the proposed algorithm showed average and maximum deviations equal to 3.2% and 11.6%, respectively, compared to the experimental, literature, and FEM

results. The validity of the kinematic assumption adopted in the proposed analytical model has been confirmed reasonably. Still, it should be noted that the velocity parameter significantly influences the overall accuracy of the ring geometry expansion prediction. When a velocity parameter greater than one is achieved, the algorithm accuracy converges and is independent of the ring geometry, the material flow stress, and the adopted process conditions. Therefore, the proposed algorithm can be utilized in the early design stages for the process engineers to investigate the influence of initial and final ring geometries, process conditions, and material properties on the geometrical expansion of the ring, which helps reduce the number of FEM simulations required for an efficient design of the profiled ring rolling process.

Appendix 1 Temperature-dependent properties of Inconel 718 and 42CrMo4 alloys

Fig. 13 Temperature-dependent Young’s modulus, thermal conductivity, and specific heat capacity properties for the Inconel 718 material

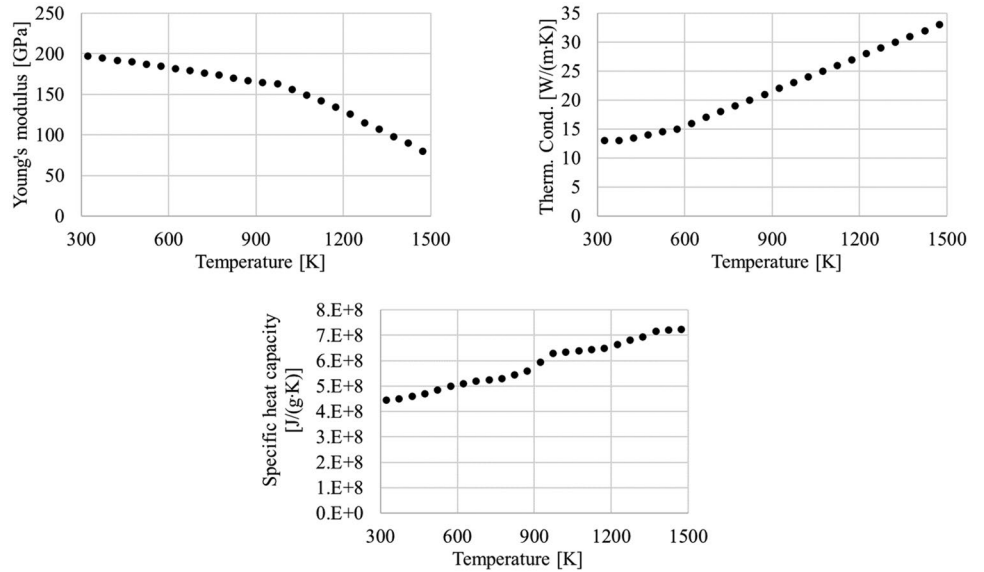
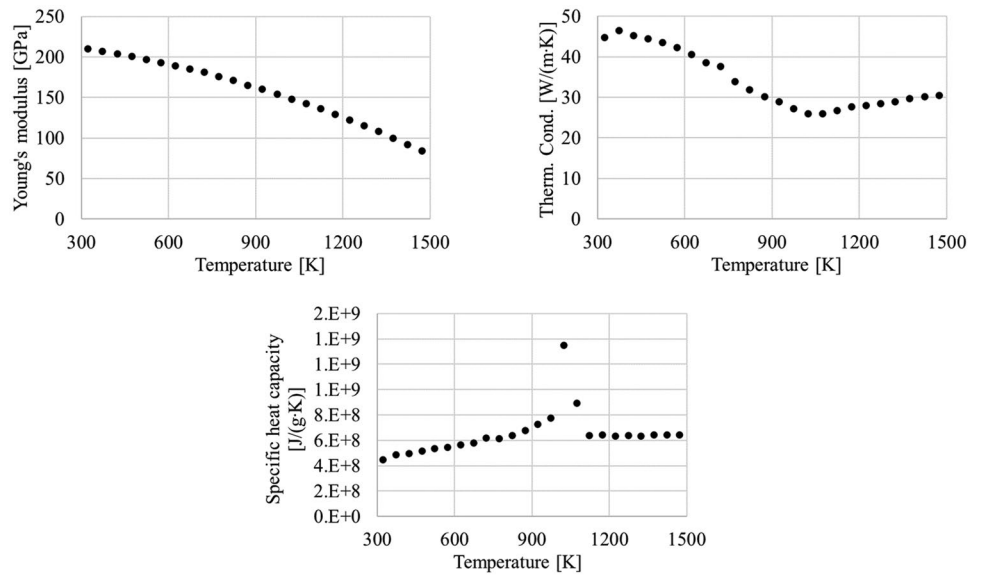


Fig. 14 Temperature-dependent Young’s modulus, thermal conductivity, and specific heat capacity properties for the 42CrMo4 material



Appendix 2 Detailed simulation levels for the process settings influence investigation (Table 2 of the paper)

Parameters	Ring#1A								
Sub-case numbering	A1-1	A1-2	A1-3	A1-4	A1-5	A1-6	A1-7	A1-8	A1-9
Main-roll rotational speed [rad/s]	2			3			4		
Initial mandrel feeding speed [mm/s]	0.26	1.88	3.33	0.4	2.86	5.08	0.54	3.85	6.84
Final mandrel feeding speed [mm/s]	0.16	1.75	3.19	0.24	2.68	4.86	0.33	3.6	6.54
Mandrel active time [s]	139	19.2	10.8	90	12.6	7.08	66.7	9.34	5.26
Total process time [s]	160	25.2	15.2	105	16.8	12.3	74.5	13.9	9.8
Parameters	Ring#2A								
Sub-case numbering	A2-1	A2-2	A2-3	A2-4	A2-5	A2-6	A2-7	A2-8	A2-9
Main-roll rotational speed [rad/s]	2			3			4		
Initial mandrel feeding speed [mm/s]	0.35	2.7	4.8	0.5	4	7.2	0.7	5.5	9.7
Final mandrel feeding speed [mm/s]	0.2	2.4	4.37	0.3	3.6	6.65	0.4	4.9	8.9
Mandrel active time [s]	140	18.15	10.21	98	12.25	6.79	70	8.91	5.05
Total process time [s]	158	22.9	15.2	108	16.5	11.2	76.3	13.6	9.7
Parameters	Ring#3A								
Sub-case numbering	A3-1	A3-2	A3-3	A3-4	A3-5	A3-6	A3-7	A3-8	A3-9
Main-roll rotational speed [rad/s]	2			3			4		
Initial mandrel feeding speed [mm/s]	0.46	3.45	6.14	0.7	5.26	9.37	0.94	7.08	12.59
Final mandrel feeding speed [mm/s]	0.28	3.22	5.87	0.43	4.92	8.96	0.58	6.62	12.05
Mandrel active time [s]	139.5	18.55	10.42	91.34	12.16	6.83	67.92	9.04	5.08
Total process time [s]	159.5	24.5	15.2	97.8	16.5	11.7	76.2	14.5	9.7

Author contribution Conceptualization (IM, LQ, GAB), methodology (IM, LQ, GAB), software (IM, MP), validation (IM, MP), formal analysis (IM, LQ, MP), investigation (IM, LQ), resources (SCR, NK, RC), data curation (IM, LQ), writing – original draft (IM, LQ), writing – review and editing (IM, LQ), visualization (IM, LQ), supervision (NK, RC), project administration (LQ, GAB, RC), funding acquisition (LQ, SCR).

Funding This research was supported by Basic Science Research Program through the National Research Foundation of Korea (NRF), funded by the Ministry of Education (2019R111A1A01062323). Prof. Dr. Luca Quagliato was supported by RP-Grant 2021 of Ewha Womans University.

Availability of data and material The data that support the findings of this study are stored in an online repository and available on request from the corresponding author [Prof. Luca Quagliato, Ph.D.].

Code availability The simulation files relevant for this research are stored in an online repository and available on request from the corresponding author [Prof. Luca Quagliato, Ph.D.].

Declarations

Ethics approval This research does not involve any human or animal participants. All professional ethics have been followed. The manuscript has not been submitted to other journals for simultaneous consideration.

Consent for publication The manuscript has not been published previously (partly or in full). No data has been fabricated or manipulated, and no data, text, or theories by others are presented as if they were the author's own. Consent to submit has been received explicitly from all co-authors. Authors whose names appear on the submission have contributed sufficiently to the scientific work and therefore share collective responsibility and accountability for the results.

Competing interests The authors declare no competing interests.

References

- Berti GA, Quagliato L, Monti M (2015) Set-up of radial–axial ring-rolling process: process work sheet and ring geometry expansion prediction. *Int J Mech Sci* 99:58–71
- Wang ZW, Fan JP, Hu DP, Tang CY, Tsui CP (2010) Complete modeling and parameter optimization for virtual ring rolling. *Int J Mech Sci* 52:1325–1333
- Mamalis AG, Hawkyard JB, Johnson W (1976) Spread and flow pattern in ring rolling. *Int J Mech Sci* 18:11–16
- Lin H, Zhi ZZ (1997) The extremum parameters in ring rolling. *J Mater Process Technol* 69:273–276
- Zhou G, Hua L, Qian DS (2011) 3D coupled thermo-mechanical FE analysis of roll size effects on the radial-axial ring rolling process. *Comput Mater Sci* 50:911–924
- Quagliato L, Berti GA (2016) Mathematical definition of the 3D strain field of the ring in the radial-axial ring rolling process. *Int J Mech Sci* 115–116:746–759
- Quagliato L, Berti GA (2017) Temperature estimation and slip-line force analytical models for the estimation of the radial forming force in the RARR process of flat rings. *Int J Mech Sci* 123
- Quagliato L, Berti GA, Kim D, Kim N (2018) Slip line model for forces estimation in the radial-axial ring rolling process. *Int J Mech Sci* 138–139:17–33
- Lim T, Pillinger I, Hartley P (1998) A finite-element simulation of profile ring rolling using a hybrid mesh model. *J Mater Process Technol* 80–81:199–205
- Davey K, Ward MJ (2002) A practical method for finite element ring rolling simulation using the ALE flow formulation. *Int J Mech Sci* 44:165–190
- Kim B, Moon H, Kim E, Choi M, Joun M (2013) A dual-mesh approach to ring-rolling simulations with emphasis on remeshing. *J Manuf Process* 15:635–643
- Kim N, Kim H, Jin K (2012) Optimal design to reduce the maximum load in ring rolling process. *Int J Precis Eng Manuf* 13:1821–1828
- Guo L, Yang H (2011) Towards a steady forming condition for radial-axial ring rolling. *Int J Mech Sci* 53:286–299
- Parvizi A, Abrinia K (2014) A two dimensional upper bound analysis of the ring rolling process with experimental and FEM verifications. *Int J Mech Sci* 79:176–181
- Anjami N, Basti A (2010) Investigation of rolls size effects on hot ring rolling process by coupled thermo-mechanical 3D-FEA. *J Mater Process Technol* 210:1364–1377
- Jenkouk V, Hirt G, Franke M, Zhang T (2012) Finite element analysis of the ring rolling process with integrated closed-loop control. *CIRP Ann - Manuf Technol* 61:267–270. <https://doi.org/10.1016/j.cirp.2012.03.115>
- Liang L, Guo L, Wang Y, Li X (2019) Towards an intelligent FE simulation for real-time temperature-controlled radial-axial ring rolling process. *J Manuf Process* 48:1–11. <https://doi.org/10.1016/j.jmapro.2019.09.032>
- Qi H, Li Y (2017) Research status and developing trends on the ring rolling process of profile ring parts. *Procedia Eng* 207:1260–1265
- Lv N, Liu D, Hu Y et al (2022) Multi-objective optimization of parametric design for profile ring rolling process based on residual stress control. *Int J Adv Manuf Technol*
- Michl D, Sydow B, Bambach M (2020) Ring rolling of pre-forms made by wire-arc additive manufacturing. *Procedia Manuf* 47:342–348
- Qian D, Zhang Z, Hua L (2013) An advanced manufacturing method for thick-wall and deep-groove ring – combined ring rolling. *J Mater Process Technol* 213:1258–1267
- Deng J, Mao H (2015) A blank optimization design method for three-roll cross rolling of complex-groove and small-hole ring. *Int J Mech Sci* 93:218–228
- Zhou P, Zhang L, Gu S, Ruan J, Teng L (2014) Mathematic modeling and FE simulation of radial-axial ring rolling large L-section ring by shape axial roll. *Int J Adv Manuf Technol* 72:729–738
- Qian DS, Hua L, Pan LB (2009) Research on gripping conditions in profile ring rolling of raceway groove. *J Mater Process Technol* 209:2794–2802
- Alfozan A, Gunasekera JS (2002) Design of profile ring rolling by backward simulation using upper bound element technique (UBET). *J Manuf Process* 4:97–108
- Qian D, Hua L (2010) Blank design optimization for stepped-section profile ring rolling. *Sci China Technol Sci* 53:1612–1619
- Zhao YM, Qian DS (2010) Effect of rolling ratio on groove-section profile ring rolling. *J Mech Sci Technol* 24:1679–1687
- Davey K, Ward MJ (2003) An ALE approach for finite element ring-rolling simulation of profiled rings. *J Mater Process Technol* 139:559–566
- Davey K, Ward MJ (2002) The practicalities of ring rolling simulation for profiled rings. *J Mater Process Technol* 125–126:619–625
- Yang DY, Kim KH, Hawkyard JB (1991) Simulation of T-section profile ring rolling by the 3-D rigid-plastic finite element method. *Int J Mech Sci* 33:541–550. [https://doi.org/10.1016/0020-7403\(91\)90016-V](https://doi.org/10.1016/0020-7403(91)90016-V)
- Xie C, Dong X, Li S, Huang S (2000) Rigid-viscoplastic dynamic explicit FEA of the ring rolling process. *Int J Mach Tools Manuf* 40:81–93. [https://doi.org/10.1016/S0890-6955\(99\)00043-7](https://doi.org/10.1016/S0890-6955(99)00043-7)

32. Kim KH, Suk HG, Huh MY (2007) Development of the profile ring rolling process for large slewing rings of alloy steels. *J Mater Process Technol* 187–188:730–733
33. Ranatunga V, Gunasekera JS, Vaze SP, De Souza U (2004) Three-dimensional UBET simulation tool for Seamless Ring Rolling of complex profiles. *J Manuf Process* 6:179–186
34. Hua L, Qian DS, Pan LB (2009) Deformation behaviors and conditions in L-section profile cold ring rolling. *J Mater Process Technol* 209:5087–5096
35. Li L, Li X, Liu J, He Z (2013) Modeling and simulation of cold rolling process for double groove ball-section ring. *Int J Adv Manuf Technol* 69:1717–1729. <https://doi.org/10.1007/s00170-013-5140-5>
36. Li L, Li X, Liu J, He Z (2015) Effects of speed parameters on cold rolling process of double groove ball-section ring. *Mat Res Inn* 19:1323–1327
37. Li L, Li X, Liu J, He Z (2016) Effects of roll sizes on uniformity of strain and variation of configuration in cold-closed T-shaped rolling process of HE30 aluminum alloy ring. *Int J Adv Manuf Technol* 86:191–201
38. Tian L, Luo Y, Mao HJ, Hua L (2013) A hybrid of theory and numerical simulation research for virtual rolling of double-groove ball rings. *Int J Adv Manuf Technol* 69:1–13
39. Kalyani A, Mattikalli A, Deshmukh A (2015) The effect of force parameter on profile ring rolling process. *Int J Eng Res V4*:840–844
40. Zhu X, Liu D, Yang Y, Hu Y, Liu G, Wang Y (2016) Effects of blank dimension on forming characteristics during conical-section ring rolling of Inco718 alloy. *Int J Adv Manuf Technol* 84:2707–2718
41. Monti M, Berti GA (2012) Design of a flanged ring produced by hot forming using FE analysis. *Int J Mat Eng Tech* 7:1–15
42. Lee KH, Ko DC, Kim DH, Lee SB, Sung NM, Kim BM (2014) Design method for intermediate roll in multi-stage profile ring rolling process: the case for excavator idler rim. *Int J Precis Eng Manuf* 15:503–512
43. Park M, Lee C, Lee J, Lee I, Joun M, Kim B et al (2016) Development of L-sectioned ring for construction machines by profile ring rolling process. *Int J Precis Eng Manuf* 17:233–240
44. Tani K, Ishigai S, Sato T, Tsumori Y (2005) The evolution of near-net-shape ring-rolling processes for large rings made of Ti-6Al-4V. *Kobelco Tech Rev* 26:43–48
45. Cleaver CJ, Arthington MR, Mortazavi S, Allwood JM (2016) Ring rolling with variable wall thickness. *CIRP Ann - Manuf Technol* 65:281–284
46. Cleaver CJ, Allwood J (2017) Incremental profile ring rolling with axial and circumferential constraints. *CIRP Ann - Manuf Technol* 66:285–288
47. Cleaver CJ, Lohmar J, Tamimi S (2021) Limits to making L-shape ring profiles without ring growth. *J Mater Process Technol* 292:117062
48. Cleaver CJ, Allwood JM (2017) Incremental ring rolling to create conical profile rings. *Procedia Eng* 207:1248–1253
49. Li X, Guo L, Liang L, Yang W (2018) Motion control of guide rolls in intelligent simulation for profiled ring rolling process. *Procedia Manuf* 15:97–104
50. Oh IY, Hwang TW, Woo YY, Yun HJ, Moon YH (2018) Analysis of defects in L-section profile ring rolling. *Procedia Manuf* 15:81–88
51. Li L, Li X, Liu J, He Z (2016) A quantitative planning method of variable feed rates for cold profiled ring rolling process. *Int J Adv Manuf Technol* 86:2585–2593
52. Kang JH (2014) Research on filling limit of profile ring rolling on circumferential surface. *Int J Emerg Tech Adv Eng* 12:40–45
53. Liang L, Guo L, Liu Z, Wang P, Zhang H (2021) On a precision forming criterion for groove-section profiled ring rolling process. *J Mater Process Technol* 296:117207
54. Quagliato L (2018) Development of procedures and analytical-numerical models for incremental forming processes of metallic materials (Ph.D. thesis, University of Padua)
55. Sun Z, Yang H, Ou X (2008) Thermo-mechanical coupled analysis of hot ring rolling process. *Trans Nonferrous Met Soc China* 18:1216–1222
56. Lohmar J, Cleaver CJ, Allwood JM (2020) The influence of constraint rolls on temperature evolution and distribution in radial ring rolling. *J Mater Process Technol* 282:116663
57. Tang X, Wang B, Zhang H, Fu X, Ji H (2017) Study on the microstructure evolution during radial-axial ring rolling of IN718 using a unified internal state variable material model. *Int J Mech Sci* 128–129:235–252
58. Thomas A, El-Wahabi M, Cabrera JM, Prado JM (2006) High temperature deformation of Inconel 718. *J Mater Process Technol* 177:469–472
59. Lee KH, Ko DC, Kim DH, Lee SB, Sung NM, Kim BM (2014) Control method for centering rolls in radial-axial ring rolling process. *Int J Precis Eng Manuf* 15:535–544
60. Schwich G, Jenkouk V, Hirt G (2019) Realistic modelling of the tool kinematics of radial-axial ring rolling machines in finite element simulation. *AIP Conf Proc* 1769:130018
61. Hensel A, Spittel T (1978) *Kraft und Arbeitsbedarf bildsamer formgebungsverfahren*, 1st edn. Deutscher Verlag für Grundstoffindustrie, Leipzig (in German language)

Publisher's Note Springer Nature remains neutral with regard to jurisdictional claims in published maps and institutional affiliations.

Springer Nature or its licensor holds exclusive rights to this article under a publishing agreement with the author(s) or other rightsholder(s); author self-archiving of the accepted manuscript version of this article is solely governed by the terms of such publishing agreement and applicable law.